Nonlinearity 6 (1993) 843–867. Printed in the UK

The collapse of an axi-symmetric, swirling vortex sheet

Russel E Caflisch†§, Xiaofan Li†‖ and Michael J Shelley‡¶

† Department of Mathematics, UCLA, Los Angeles, CA 90024, USA

‡ Courant Institute of Mathematical Sciences, New York, NY 10012, USA

Received 24 November 1992

Recommended by D Meiron

Abstract. An axi-symmetric and swirling vortex sheet is investigated as the simplest flow in which there is non-trivial vortex stretching and as a possible setting for studying vortex cancellation and singularity formation. Rayleigh's criterion indicates linear stability of a single sheet but instability for other configurations of sheets. Due to the simplicity of vortex sheet problems, the linear modes and growth rates (or frequencies) can be explicitly expressed. Subsequent nonlinear evolution is numerically simulated using a vortex method. The numerical results for an axi-symmetric swirling sheet with a vortex line along the axis of symmetry show detachment of a vortex ring from the sheet into the outer fluid, and collapse of the sheet onto the vortex line at some points. Vortex cancellation, which in the presence of viscosity would likely lead to vortex line reconnection, seems to occur in both of these phenomena. The evolution of two co-axial, axi-symmetric, swirling vortex sheets is similar.

PACS numbers: 0340G, 4720, 4730

1. Introduction

Axi-symmetric flow with swirl for an inviscid incompressible fluid is the simplest flow that allows non-trivial vortex stretching. The flow description is further simplified if the vorticity is concentrated on an axi-symmetric surface; that is, a flow induced by a vortex sheet (or more than one sheet).

The restriction to axi-symmetry and to vortex sheets provides the simplest setting in which to examine nonlinear processes such as vortex cancellation and singularity formation. For similar reasons, there have been a number of recent computational studies of smooth axi-symmetric flow with swirl [3, 11, 16, 22]. Furthermore in the present study, a new phenomenon, the pinching and collapse of a vortex sheet, is exhibited.

These flows represent a significant idealization, since the restriction to axi-symmetry for a swirling vortex sheet suppresses the dominant Kelvin–Helmholtz instability, which is not axi-symmetric. The resulting flows, however, are quite similar in appearance to those generated by the impulsive rotation of a cylinder [7, 12, 31]. This gives us some confidence that the phenomena studied here are of physical significance, in addition to their basic mathematical importance.

§ *Research supported in part by the National Science Foundation through grant number NSF-DMS-9005881.*

‖ Research supported in part by a UCLA Chancellor's Fellowship and by the National science Foundation through grant number NSF-DMS-9005881.

¶ Research supported in part by the National Science Foundation through grant number DMS-9100383, and by the Department of the Air Force through grant number F-49620-02-J-0023F.

0951-7715/93/060843+25$07.50

An axi-symmetric swirling vortex sheet with circulation Γ can be represented by the cylindrical coordinates $(z(\alpha,t), r(\alpha,t), \psi(\alpha,t))$ of a vortex line on the sheet, in which α is a 'Lagrangian' parameter along the vortex line. The full sheet is formed by rotating this curve around the axis of symmetry $r = 0$. The evolution of the sheet is governed by the following integro-differential equations [5]:

$$\partial_t z(\alpha,t) = \frac{\Gamma}{2\pi^2} PV \int I_1(r, r', z-z', \psi')\, d\alpha' \tag{1.1}$$

$$\partial_t r(\alpha,t) = \frac{\Gamma}{2\pi^2} PV \int I_2(r, r', z-z', \psi')\, d\alpha' \tag{1.2}$$

$$\partial_t \psi(\alpha,t) = \Gamma(4\pi r^2)^{-1} \tag{1.3}$$

(sign errors in the r, z equations in (5.11) have been corrected) in which

$$\begin{aligned} I_1(r, r', \Delta z, \psi') &= r'\psi'_\alpha \left(\frac{m}{4rr'}\right)^{3/2} \left(\frac{r'-r}{1-m}E - \frac{2r}{m}(E-K)\right) \\ I_2(r, r', \Delta z, \psi') &= r'\psi'_\alpha \Delta z \left(\frac{m}{4rr'}\right)^{3/2} \left(\frac{2}{m}(E-K) + \frac{1}{1-m}E\right). \end{aligned} \tag{1.4}$$

In these equations r' and ψ' denote $r(\alpha')$ and $\psi(\alpha')$, etc, and $E = E(m)$ and $K = K(m)$ are the elliptic integrals of the first kind evaluated at

$$m = \frac{4rr'}{\Delta z^2 + (r+r')^2}. \tag{1.5}$$

They account for the integration of the vortex interaction around a circle of symmetry. The integrals in (1.1) and (1.2) have singular integrands at $\alpha' = \alpha$ and are interpreted in the Cauchy principal value sense. The simplicity of the angular velocity equation is because the circulation ru_θ is constant in each irrotational region of an axi-symmetric flow, i.e. $ru_\theta = 0$ inside the sheet and $ru_\theta = \Gamma/2\pi$ outside the sheet, and because the velocity u of the sheet (at fixed α) is the average $u = \frac{1}{2}(u_+ + u_-)$ of the limiting velocities u_+ and u_- on either side of the sheet. The system (1.1)–(1.3) is analogous to the Lagrangian description of two-dimensional vortex sheet dynamics through the Birkhoff–Rott integral. The generalization of (1.1)–(1.3) to configurations of more than one sheet is straightforward. For the case of an axi-symmetric vortex sheet without swirl, these equations were derived earlier by de Bernardinis and Moore [9] and used in [8, 19–21].

The steady-flow solution $(z, r, \psi) = (\alpha, R, t\Gamma/(4\pi R^2))$ for (1.1)–(1.3) is linearly stable to axi-symmetric disturbances, but flows with multiple vortex sheets can be linearly unstable, as described in section 2. In order to investigate the subsequent nonlinear evolution, a numerical method for solving the vortex sheet equations (1.1)–(1.3) is formulated in section 3.

The numerical method is applied first to the (linearly) stable configuration of a single axi-symmetric swirling vortex sheet in section 4. For small amplitude perturbations, the oscillation of the sheet agrees with the linear theory; while for larger amplitude the resulting outward flow leads to a curvature singularity and rollup of the sheet, which cannot be reversed, so that the flow loses its temporal periodicity.

The simplest linearly unstable configuration consists of an axi-symmetric vortex sheet combined with a vortex line on the axis of symmetry. According to Rayleigh's criterion (re-derived through a kinematic argument at the end of section 2) this flow is unstable if

$$|\Gamma_2| < |\Gamma_1| \tag{1.6}$$

in which Γ_1 is the circulation inside the sheet and Γ_2 is the circulation outside the sheet; i.e. Γ_1 is the strength of the vortex line and $\Gamma_2 - \Gamma_1$ is the strength of the sheet. The numerical computations presented in section 5 for the resulting nonlinear evolution show formation of outward and inward jets along the sheet, detachment of a vortex ring from the sheet into the outer fluid, and collapse of the sheet onto the vortex line at some points. The intense winding-up of the sheet as it collapses prevents accurate computation past a certain time before the sheet hits $r = 0$. Extrapolation of the results, however, seems to indicate that in a finite time there is a collision and cancellation between the sheet and the vortex line, as well as a collision between the sheet and itself during the detachment of the outer ring. In the presence of viscosity, this would lead to the breaking and reconnection of vortex lines (see [26] for example). Rayleigh [23] also noted the analogy between the stability of axisymmetric flows and the stability of density stratified two-dimensional flows. However, while some of the structures observed here are very similar to those seen in simulations of the Rayleigh–Taylor instability (see [30] for example), very nonlinear phenomena such as collapse of the sheet onto the axis of symmetry are quite specific to axisymmetric flows.

For two co-axial axi-symmetric vortex sheets with swirl, the instability criterion is the same as (1.6) and the subsequent nonlinear evolution is also similar if the inner radius is not too large, as shown in section 6. As before the outer sheet collapses onto the inner sheet at some points. Unlike the previous case no collapse onto the axis is observed.

Conclusions from this investigation are presented in section 7.

2. Linear stability analysis for axi-symmetric vortex sheets

On a cylindrical vortex sheet with pure swirling flow, the vortex lines are straight lines in the $\hat{z}$ direction. The Kelvin–Helmholtz instability for this steady flow is then in the x–y plane, and so it is not excited by perturbations that are axi-symmetric. In this section a linearized stability analysis is presented for axi-symmetric perturbations of cylindrical sheets in several configurations.

Rayleigh's criterion [10] provides a necessary and sufficient criterion for linear stability of a steady swirling flow to axi-symmetric perturbations; namely the flow is stable if and only if the square of the circulation is a non-decreasing function of the radius. The results of this section are of course consistent with Rayleigh's criterion, but for these vortex sheet problems, explicit expressions are found for the linear modes and for the dispersion relation. At the end of this section, a kinematic argument for stability or instability of a vortex sheet is presented, as an alternative to the usual dynamic argument in the derivation of Rayleigh's criterion.

Two vortex sheet configurations are considered. First is the case of a single, axi-symmetric vortex sheet with a vortex line along the axis. Second, to give the inner flow more degrees of freedom, the vortex line is replaced by an inner vortex sheet. The linearized analysis is performed in the Eulerian variables and follows that of Rotunno [24] for a single axi-symmetric sheet. A related stability analysis for a swirling vortex sheet within an annulus is given in [3].

2.1. Cylindrical vortex sheet and a vortex line

Consider a vortex line of circulation Γ_1 on the axis of symmetry, contained inside a cylindrical vortex sheet so that combination has circulation Γ_2. Axi-symmetric perturbations will not alter the position of the vortex line. The velocity potential in Eulerian variables for this flow will be

$$\phi = \begin{cases} \phi_1(z,r,t) + \theta\Gamma_1/2\pi & \text{inside the sheet} \\ \phi_2(z,r,t) + \theta\Gamma_2/2\pi & \text{outside} \end{cases} \tag{2.1}$$

and the sheet position is

$$r = R_0 + \xi(z,t). \tag{2.2}$$

These satisfy the Eulerian fluid equations

$$\nabla^2\phi_1 = 0 \qquad \nabla^2\phi_2 = 0 \tag{2.3}$$

inside and outside the sheet, with jump conditions that the normal velocity and pressure are continuous, i.e.,

$$\phi_{1r} = \xi_t + \phi_{1z}\xi_z \tag{2.4}$$

$$\phi_{2r} = \xi_t + \phi_{2z}\xi_z \tag{2.5}$$

$$\phi_{1t} + \frac{1}{2}\left(\frac{\Gamma_1/2\pi}{R+\xi}\right)^2 + \frac{1}{2}\phi_{1z}^2 + \frac{1}{2}\phi_{1r}^2 = \phi_{2t} + \frac{1}{2}\left(\frac{\Gamma_2/2\pi}{R+\xi}\right)^2 + \frac{1}{2}\phi_{2z}^2 + \frac{1}{2}\phi_{2r}^2. \tag{2.6}$$

The linearized free boundary equations are then

$$\begin{aligned} &\phi_{1r} = \xi_t \\ &\phi_{2r} = \xi_t \\ &\phi_{1t} - \frac{(\Gamma_1/2\pi)^2}{R_0^3}\xi = \phi_{2t} - \frac{(\Gamma_2/2\pi)^2}{R_0^3}\xi. \end{aligned} \tag{2.7}$$

The kth mode for (2.3) is

$$\begin{aligned} \phi_1 &= b_1 I_0(|k|r)e^{ikz+\sigma t} \\ \phi_2 &= b_2 K_0(|k|r)e^{ikz+\sigma t} \\ \xi &= e^{ikz+\sigma t} \end{aligned} \tag{2.8}$$

in which I_0 and K_0 are the modified Bessel functions [1] and b_1, b_2 and σ will be determined from the linearized free boundary conditions (2.7). Since $I_0' = I_1$ and $K_0' = -K_1$, these equations become

$$\begin{aligned} &b_1|k|I_{10} = \sigma \\ &-b_2|k|K_{10} = \sigma \\ &\sigma b_1 I_{00} - R_0^{-3}(\Gamma_1/2\pi)^2 = \sigma b_2 K_{00} - R_0^{-3}(\Gamma_2/2\pi)^2. \end{aligned} \tag{2.9}$$

in which $I_{00} = I_0(|k|R_0)$, $I_{10} = I_1(|k|R_0)$, etc. Since $I_0(x)K_1(x) + I_1(x)K_0(x) = \frac{1}{x}$, it follows that

$$\sigma = \pm(2\pi)^{-1}(\Gamma_1^2 - \Gamma_2^2)^{1/2}|k|R_0^{-1}\sqrt{I_{10}K_{10}} \tag{2.10}$$

$$\begin{aligned} b_1 &= \pm(2\pi)^{-1}(\Gamma_1^2 - \Gamma_2^2)^{1/2}R_0^{-1}\sqrt{K_{10}/I_{10}} \\ b_2 &= \mp(2\pi)^{-1}(\Gamma_1^2 - \Gamma_2^2)^{1/2}R_0^{-1}\sqrt{I_{10}/K_{10}}. \end{aligned} \tag{2.11}$$

This shows that the configuration of a vortex line inside a cylindrical vortex sheet is *unstable* if and only if

$$\Gamma_1^2 > \Gamma_2^2 \tag{2.12}$$

in agreement with Rayleigh's criterion. For large wavenumber k, the growth (or decay) rate is approximately

$$\sigma = \pm(2\pi)^{-1}(\Gamma_1^2 - \Gamma_2^2)^{1/2}\sqrt{|k|/2R_0^3}. \tag{2.13}$$

The linear growth rate σ as a function of $\sqrt{k}$ is plotted in figure 2.1(a), for the unstable configuration of a vortex sheet and line vortex with $\Gamma_1 = 6.0$, $\Gamma_2 = 2\pi - 6$ and $R_0 = 1.0$. This is the same configuration for which the nonlinear evolution is computed in section 5.

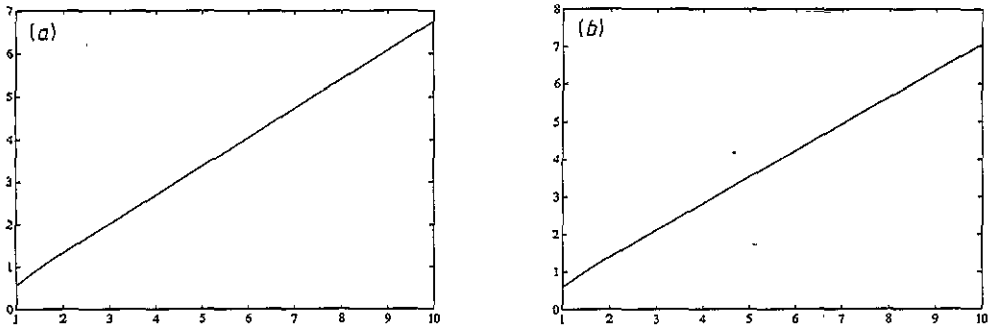

Figure 2.1. The linear growth rate σ as a function of $\sqrt{k}$ for two unstable vortex sheet configurations: (a) a cylindrical vortex sheet and line vortex with $\Gamma_1 = 6.0$, $\Gamma_2 = 2\pi - 6$ and $R_0 = 1.0$; (b) Two concentric cylindrical vortex sheets with $\Gamma_1 = -2\pi$, $\Gamma_2 = 0.0$, $R_1 = 0.1$ and $R_2 = 1.0$. Note that the growth rate is nearly a constant times $\sqrt{k}$. These are the same configurations for which the nonlinear evolutions are computed in figures 5.1–5.10 and 6.1–6.10 respectively.

2.2. *Concentric, cylindrical vortex sheets*

Consider two cylindrical vortex sheets of radius R_1 and R_2 with zero circulation inside the inner sheet, circulation Γ_1 in the region between the sheets and Γ_2 outside the outer sheet. The potential is then

$$\phi = \begin{cases} \phi_0(r,z,t) & \text{inner} \\ \phi_1(r,z,t) + \theta\Gamma_1/2\pi & \text{middle} \\ \phi_2(r,z,t) + \theta\Gamma_2/2\pi & \text{outer.} \end{cases} \tag{2.14}$$

The perturbed sheet positions are

$$r = r_1 = R_1 + \xi_1(z,t) \qquad r = r_2 = R_2 + \xi_2(z,t). \tag{2.15}$$

The linearized jump conditions are

$$\phi_{0r} = \xi_{1t} \qquad \phi_{1r} = \xi_{1t} \qquad \phi_{0t} = \phi_{1t} - R_1^{-3}(\Gamma_1/2\pi)^2\xi_1 \tag{2.16}$$

on $r = R_1$ and

$$\begin{aligned} &\phi_{1r} = \xi_{2t} \\ &\phi_{2r} = \xi_{2t} \\ &\phi_{1t} - R_2^{-3}(\Gamma_1/2\pi)^2\xi_2 = \phi_{2t} - R_2^{-3}(\Gamma_2/2\pi)^2\xi_2 \end{aligned} \tag{2.17}$$

on $r = R_2$. The linearized mode is

$$\begin{aligned} \phi_0 &= b_1 I_0(|k|r)e^{ikz+\sigma t} \\ \phi_1 &= (b_2 I_0(|k|r) + b_3 K_0(|k|r))e^{ikz+\sigma t} \\ \phi_2 &= b_4 K_0(|k|r)e^{ikz+\sigma t} \\ \xi_1 &= b_5 e^{ikz+\sigma t} \\ \xi_2 &= e^{ikz+\sigma t}. \end{aligned} \tag{2.18}$$

After substitution in (2.16) and (2.17) and some manipulation, the dispersion relation is found to be

$$\sigma^4 + (I_{11}K_{11}G_1 + I_{12}K_{12}G_2)k^2\sigma^2 + G_1G_2I_{11}K_{12}(I_{12}K_{11} - I_{11}K_{12})k^4 = 0 \tag{2.19}$$

in which

$$G_1 = (\Gamma_1/2\pi R_1)^2 \qquad G_2 = (\Gamma_2^2 - \Gamma_1^2)/(2\pi R_2)^2 \tag{2.20}$$

and $I_{11} = I_1(|k|R_1)$, $I_{12} = I_1(|k|R_2)$, etc. As in Rayleigh's criterion, the dispersion relation (2.19) has a root σ with $Re(\sigma) > 0$, corresponding to instability, if and only if $\Gamma_1^2 > \Gamma_2^2$, i.e. $G_2 < 0$.

The coefficients for the linear mode are

$$\begin{aligned} b_1 &= (\sigma/|k|I_{11})b_5 \\ b_2 &= -(|k|/\sigma)G_2K_{12} \\ b_4 &= -(\sigma/|k|K_{12}) \\ b_3 &= -(|k|/\sigma)G_2I_{12} - (\sigma/|k|)K_{12}^{-1} \\ b_5 &= (|k|/\sigma)(b_2I_{11} - b_3K_{11}) \\ &= -(|k|/\sigma)^2(I_{11}K_{12} - K_{11}I_{12})G_2 + K_{11}/K_{12}. \end{aligned} \tag{2.21}$$

The linear growth rate σ as a function of $\sqrt{k}$ is plotted in figure 2.1(b), for the unstable configuration of two concentric cylindrical vortex sheets with $\Gamma_1 = -2\pi$, $\Gamma_2 = 0.0$, $R_1 = 0.1$ and $R_2 = 1.0$. This is the same configuration for which the nonlinear evolution is computed in section 6.

2.3. *Lagrangian modes*

As detailed above, the Eulerian description of a vortex sheet consists of a radius $r = R(z,t)$ and a potential $\phi = \phi(z,r,\theta,t)$. On the other hand the Lagrangian description used in the Birkhoff–Rott equation in section 1, consists of cylindrical coordinates $(z(\alpha,t), r(\alpha,t), \psi(\alpha,t))$ for a vortex filament on the sheet. The linearization of the integro-differential equation for the Lagrangian description of the sheet is much more difficult than the linearization of the Eulerian description. These Eulerian results will now be translated into Lagrangian form.

The relation between these descriptions is that the Lagrangian position moves at the average of the velocities on either side of the sheet, i.e.

$$(z_t, r_t, r\psi_t) = \tfrac{1}{2}\{(\phi_z^+, \phi_r^+, r^{-1}\phi_\theta^+) + (\phi_z^-, \phi_r^-, r^{-1}\phi_\theta^-)\} \tag{2.22}$$

in which ϕ^+ and ϕ^- are the potentials evaluated at the vortex sheet point (z,r,ψ) from either side.

For each of the vortex sheet flows above, we will now determine the Lagrangian description for both the steady state and a linearized mode. Set the potential to be

$$\Phi = \bar{\phi} + \phi \tag{2.23}$$

in which $\bar{\phi}$ is the basic steady flow and ϕ is a perturbation. Similarly set the Lagrangian coordinates to be

$$(Z, R, \Psi) = (\bar{z}, \bar{r}, \bar{\psi}) + (z, r, \psi). \tag{2.24}$$

Since $\bar{\phi}_z = \bar{\phi}_r = 0$ in all of the flows above, the steady solution satisfies

$$(\bar{z}_t, \bar{r}_t, \bar{\psi}_t) = (0, 0, \tfrac{1}{2}R^{-2}(\bar{\phi}_\theta^+ + \bar{\phi}_\theta^-)) \tag{2.25}$$

The linearized terms in (2.22) come from two sources, the perturbation ϕ of the potential and the perturbation ξ of the interface. Since $\bar{\phi}_{\theta r} = \phi_\theta = 0$, then the perturbation velocity is

$$\begin{aligned} z_t &= \tfrac{1}{2}(\phi_z^+ + \phi_z^-) \\ r_t &= \tfrac{1}{2}(\phi_r^+ + \phi_r^-) \\ \psi_t &= -\bar{R}^{-3}(\bar{\phi}_\theta^+ + \bar{\phi}_\theta^-)\xi. \end{aligned} \tag{2.26}$$

2.3.1. Lagrangian modes for a sheet and line. The steady fluid flow corresponds to a vortex filament on the sheet with

$$(\bar{z}, \bar{r}, \bar{\psi}) = (\alpha, R_0, tR_0^{-2}(\Gamma_1 + \Gamma_2)/4\pi). \tag{2.27}$$

The equations for the linearized mode (z, r, ψ) are

$$\begin{aligned} \partial_t z &= \tfrac{1}{2}(\phi_{1z} + \phi_{2z}) \qquad (r = R_0, z = \alpha) \\ &= \tfrac{1}{2}ik(b_1 I_{00} + b_2 K_{00})e^{ik\alpha+\sigma t} \\ \partial_t r &= \tfrac{1}{2}(\phi_{1r} + \phi_{2r}) \qquad (r = R_0, z = \alpha) \\ &= \tfrac{1}{2}|k|(b_1 I_{10} - b_2 K_{10})e^{ik\alpha+\sigma t} \\ \partial_t \psi &= -((\Gamma_1 + \Gamma_2)/2\pi)R_0^{-3}e^{ik\alpha+\sigma t} \end{aligned} \tag{2.28}$$

which has solution

$$(z, r, \psi) = (\hat{z}, \hat{r}, \hat{\psi})e^{ik\alpha+\sigma t} \tag{2.29}$$

with $\hat{z}, \hat{r}, \hat{\psi}$ given by

$$\begin{aligned}
\hat{z} &= \frac{ik}{2\sigma}(b_1 I_{00} + b_2 K_{00}) \\
\hat{r} &= \frac{|k|}{2\sigma}(b_1 I_{10} - b_2 K_{10}) \\
\hat{\psi} &= -\frac{1}{\sigma} R_0^{-3}(\Gamma_1 + \Gamma_2)/2\pi
\end{aligned} \tag{2.30}$$

in which $I_{10} = I_1(|k|R_0)$, etc, and b_1, b_2 are defined in (2.11).

Note that the period of the swirling flow is found from (2.27) to be $T_0 = 8\pi^2 R_0^2/(\Gamma_1 + \Gamma_2)$ whereas the period of the oscillation for the linearized mode (in the stable problem) is $T_1 = 2\pi/|\sigma|$. Since these will differ in general, a vortex line will not return to its original position after one oscillation but will be shifted by a finite angle.

2.3.2. Lagrangian mode for two sheets. Now there are two vortex sheets with two filaments $(z_1, r_1, \psi_1)(\alpha, t)$ and $(z_2, r_2, \psi_2)(\alpha, t)$. In the steady flow these are

$$\begin{aligned}
(\bar{z}_1, \bar{r}_1, \bar{\psi}_1) &= (\alpha, R_1, tR_1^{-2}\Gamma_1/4\pi) \\
(\bar{z}_2, \bar{r}_2, \bar{\psi}_2) &= (\alpha, R_2, tR_2^{-2}(\Gamma_1 + \Gamma_2)/4\pi).
\end{aligned} \tag{2.31}$$

The linearized mode is

$$\begin{aligned}
(z_1, r_1, \psi_1) &= (\hat{z}_1, \hat{r}_1, \hat{\psi}_1)e^{ik\alpha+\sigma t} \\
(z_2, r_2, \psi_2) &= (\hat{z}_2, \hat{r}_2, \hat{\psi}_2)e^{ik\alpha+\sigma t}
\end{aligned} \tag{2.32}$$

in which

$$\begin{aligned}
\hat{z}_1 &= i(k/2\sigma)((b_1 + b_2)I_{01} + b_3 K_{01}) \\
\hat{r}_1 &= (|k|/2\sigma)((b_1 + b_2)I_{11} - b_3 K_{11}) \\
\hat{\psi}_1 &= -(1/\sigma)R_1^{-3}\Gamma_1/2\pi \\
\hat{z}_2 &= i(k/2\sigma)(b_2 I_{02} + (b_3 + b_4)K_{02}) \\
\hat{r}_2 &= (|k|/2\sigma)(b_2 I_{12} - (b_3 + b_4)K_{12}) \\
\hat{\psi}_2 &= -(1/\sigma)R_2^{-3}(\Gamma_1 + \Gamma_2)/2\pi.
\end{aligned} \tag{2.33}$$

2.4. Kinematic argument for linearized stability

The motion of vortex filaments is best described through a kinematic, rather than a dynamic, description. Here we present a kinematic derivation of the stability or instability for the vortex sheet configurations described above.

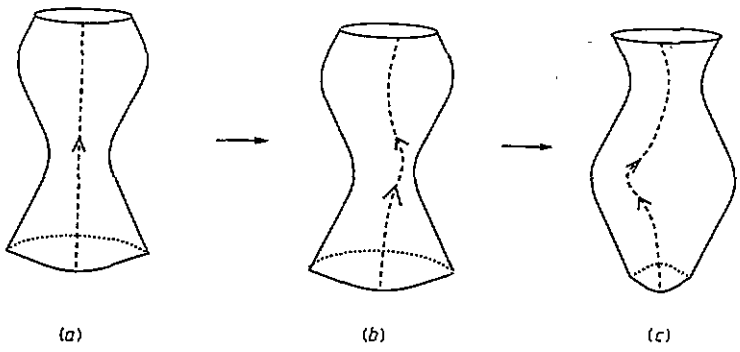

Figure 2.2. Oscillation of a single perturbed cylindrical vortex sheet with positive swirl. The broken curve is a vortex line on the sheet. A vortex line with constant angle θ in the initial data (a) will be wrapped around the sheet in the positive θ direction as in (b), due to increased angular velocity in a pinched region. The azimuthal vorticity generated by this stretching causes the vortex sheet to bulge out and the vortex lines to then wrap around the sheet in the opposite direction.

Consider first a single cylindrical vortex sheet with vorticity in the $\hat{z}$ direction and perturb its shape by a small sinusoidal perturbation, as drawn in figure 2.2(a).

Since the circulation $r^2\psi_t$ is constant, then the angular velocity is larger where the sheet is pinched. This differential rotation rate can also be thought of as a result of vorticity in the $\hat{r}$ direction. It stretches out the vortex lines in the positive $\hat{\theta}$ direction in pinched regions, as indicated in figure 2.2(b). The resulting angular vorticity is in the $\hat{\theta}$ direction below the centre of the pinch and in the $-\hat{\theta}$ direction above the centre. This angular vorticity produces an axial flow into the pinched region from below and from above. This inward flow continues until the pinched region bulges out, which causes the vortex lines to wrap up in the $-\hat{\theta}$ direction as in figure 2.2(c). The resulting angular vorticity then produces axial flow out of the pinched region. This eventually causes the bulged region to become pinched again, and the sheet returns to the state in figure 2.2(b). In this process there will be a phase lag between the bulging and pinching of the sheet and the wrapping and unwrapping of the vortex lines. This argument shows that a single vortex sheet is stable.

The same reasoning can be applied to the vortex sheet with a vortex line as section 2.2 and drawn in figure 2.3(a). The angular velocity of the sheet is $\psi_t = R^{-2}(\Gamma_1 + \Gamma_2)/2$. If $\Gamma_1^2 > \Gamma_2^2$, then the circulation Γ_1 of the line is of opposite sign to the circulation Γ_s of the sheet, since $\Gamma_s = \Gamma_2 - \Gamma_1$. Moreover the vortex lines will now wrap up the opposite direction to those for a single sheet, since sign $(\Gamma_1 + \Gamma_2) = -\text{sgn}(\Gamma_s)$. As shown in figure 2.3(b), this produces an outward flow away from the pinched region on the sheet, causing it to pinch further. Therefore the sheet is unstable in this flow.

3. Numerical methods

In this section we discuss the numerical methods used to evolve the vortex sheet whose motion is given by (1.1)–(1.3). Numerical issues that must be carefully addressed include the implementation of axial periodicity, the evaluation of singular integrals, the consequences and treatment of singularity formation, and the resolution of vortex line complexity.

Denote $z = \alpha + \bar{z}$. If at $t = 0$ the data $r(\alpha)$, $\psi(\alpha)$, and $\bar{z}(\alpha)$ are 2π-periodic, then this axial periodicity will be preserved by the subsequent motion. For a two-dimensional planar

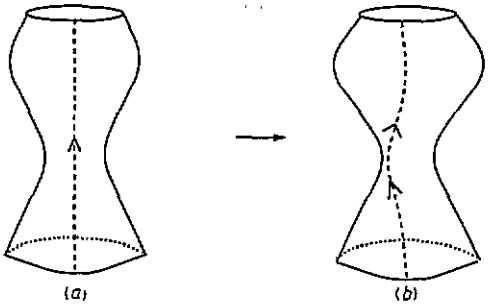

Figure 2.3. For a perturbed vortex sheet with a strong negative vortex line (not drawn) on the axis of symmetry, an initial vortex line (a) is stretched in the negative θ direction along the pinched region of the sheet. The azimuthal vorticity generated by this stretching causes the vortex sheet to pinch further and thus the stretching to increase as in (b).

vortex sheet with periodic data (sheet strength and displacement) the Birkhoff–Rott integral over R can be resummed to yield an integral over $[0, 2\pi]$ with a modified but explicitly given kernel [14]. An exact resummation is not known for the velocity integrals in (1.1) and (1.2), and a velocity integral $I(\alpha)$ is instead approximated by the symmetric truncation

$$I_M(\alpha) = PV \int_{\alpha-(M+\frac{1}{2})2\pi}^{\alpha+(M+\frac{1}{2})2\pi} f(\alpha, \alpha')\, d\alpha'. \tag{3.1}$$

The range of integration is thus $2M + 1$ periods of the data $(r, \bar{z}, \psi)$. By centring the range of integration at α, $I_M(\alpha)$ is a 2π-periodic function, as is $I(\alpha)$, and the integral need only be evaluated for $0 \leqslant \alpha \leqslant 2\pi$. Moreover, the convergence of $I_M(\alpha)$ to $I(\alpha)$ is rapid. Using the periodicity of the data, the symmetry of truncation, and the small m behaviour of $E(m)$ and $K(m)$, it can be shown that

$$I(\alpha) = I_M(\alpha) + \mathcal{O}\left(\left(\frac{l_r}{l_z}\frac{1}{M}\right)^4\right) \tag{3.2}$$

for large M, where l_r is a characteristic radius of the sheet, and l_z the periodicity length along z (here set to 2π). For the calculations presented here $M = 4$ (9 periods) was found to be sufficient. Further increases in M gave no significant changes in the results.

From the initial instability of the sheet the first significant event is the formation of a singularity, which is apparently related to those seen in 2D vortex sheet motion [14, 15, 17, 18, 25]. We seek to compute the sheet motion accurately up to this first singularity time and then beyond it. One consideration must be the accurate quadrature of the singular velocity integrals. The limit $\alpha' \to \alpha$ gives $m \to 1^-$, for which both integrands are singular. For simplicity consider $\alpha = 0$. Then either velocity integrand can be written in the form

$$f(\alpha') = H_1(\alpha') + \frac{H_2(\alpha')}{\alpha'} + H_3(\alpha') \log|\alpha'| \tag{3.3}$$

where the functions $H_i(\alpha')$ are smooth if the data $(r, \bar{z}, \psi)$ are smooth. The pole singularity has a well defined principal value integral, while the remainder is absolutely integrable. Sidi and Israeli [28] have developed generalizations of the Euler–MacLaurin error expansion

for trapezoidal rule approximations to such singular integrals. Let $\sum''_{k=j_1}^{j_2} a_k$ denote the 'trapezoidal rule' sum in which the endpoints a_{j_1} and a_{j_2} are both weighted by $\frac{1}{2}$. Let the α-interval $[-\pi, \pi]$ be discretized uniformly by $N+1$ points (including endpoints) where N is even. Then $2\bar{N} = (2M+1)N + 1$ is the total number of quadrature points of $[-L, L]$, where $L = (M + \frac{1}{2})2\pi$. Then the trapezoidal rule approximation to $I_M(0)$, which omits the singular point (at $\alpha = 0$), has the leading order errors [28]

$$E^h = I_M - I_M^h = PV \int_{-L}^{L} f(\alpha')\,d\alpha' - h \sum_{\substack{k=-\bar{N} \\ k\neq 0}}^{\bar{N}}{}'' f(kh)$$

$$= -\tfrac{1}{12}(f'(L) - f'(-L))h^2 + H_2'(0)h - \ln(2\pi)H_3(0)h + H_3(0)h\log h + \mathcal{O}(h^3) \tag{3.4}$$

where $h = 2\pi/N$. The first term is usually associated with the Euler–MacLaurin expansion for smooth integrands (cf [29]), while the others are associated with the singularities of the integrand. The Richardson extrapolation $\tilde{I}_M^h = 2I_M^h - I_M^{2h}$ removes the $\mathcal{O}(h)$ error terms, and the quadrature formula becomes an alternate point quadrature rule over odd indices, or equivalently the mid-point rule over cells of length $2h$. That is

$$\begin{aligned}\tilde{E}^h &= I_M - \tilde{I}_M^h \\ &= PV \int_{-L}^{L} f(\alpha')\,d\alpha' - 2h \sum_{\substack{k=-\bar{N} \\ k \text{ odd}}}^{\bar{N}} f(kh) \\ &= \tfrac{1}{6}(f'(L) - f'(-L))h^2 - 2H_3(0)\ln(2)h + \mathcal{O}(h^3).\end{aligned} \tag{3.5}$$

For the velocity integrands of (1.1), (1.2), $H_3(0)$ is easily calculated. For (1.1), we have $H_3(0) = -(\Gamma/2\pi^2)(\psi_\alpha(0)/4r(0))$, while $H_3(0) = 0$ for (1.2). Thus, the overall quadrature error is made $\mathcal{O}(h^2)$ by the calculation of $H_3(0)$ and the explicit removal of the remaining $\mathcal{O}(h)$ error term in (3.5). For 2D planar sheets the alternate point quadrature is of infinite order, and was used successfully by Shelley [25] in the study of singularity formation.

The higher order of the alternate point quadrature given in (3.5) (together with the explicit error correction) depends upon the smoothness of $(r, \bar{z}, \psi)$ and requires uniform discretization in α. The initial discretization in α is thus chosen to be on a uniform grid. Derivatives with respect to α are approximated to fourth order using splines, and the overall quadrature error is effectively of order $\mathcal{O}(h^3)$ since $|f'(L) - f'(-L)|h^2$ is small compared with $\mathcal{O}(h^3)$. Time integration is accomplished by Hamming's method, a fourth-order predictor–corrector method which requires only two velocity evaluations (each of which is $\mathcal{O}(N^2)$) per time step.

Another aspect of the evolution which must be dealt with is its linear ill posedness. The linear analysis of the previous section gives the growth rate

$$\sigma_k^2 \sim |k|. \tag{3.6}$$

The unboundedness of this linear growth rate causes the rapid and spurious growth of round-off induced noise at the smallest scales, as they have the fastest growth rates. This phenomenon has been well studied for the motion of 2D planar sheets. Krasny [14] controlled this spurious behaviour by using a nonlinear Fourier filter at every time step. It sets to zero

any Fourier coefficient of the data with magnitude less than some given filter level. For example for the function $r(\alpha)$, the discrete Fourier transform $\hat{r}_n$ is modified at the beginning of every time step by the assignment

$$\hat{r}_n \leftarrow \begin{cases} \hat{r}_n & \text{if } |\hat{r}_n| > \varepsilon \\ 0 & \text{if } |\hat{r}_n| < \varepsilon. \end{cases} \tag{3.7}$$

In these calculations, ε lies in the range 10^{-12}–10^{-11}, i.e. near the level of the round-off error. In short, if the calculation is well resolved, so that the highest modes have amplitude near the round-off error, these amplitudes are set to zero at each time step. This filter prevents spurious growth of roundoff error in the high wavenumber modes, but it allows the correct growth of these modes due to nonlinearities. Convergence of such a method, when combined with the alternate point quadrature as used by Shelley [25], has been proved by Caflisch *et al* [4]. This concludes the discussion of the methods used before the first singularity time.

As is the case for 2D planar sheets, a regularization of vortex sheet motion is apparently necessary to investigate the behaviour of the sheet past the singularity time [13]. Different approaches can be taken [2], but the most convenient regularization, which preserves the sheet description of the flow, is to mollify the singularities in the integrands [13, 27]. We introduce a smoothing parameter δ and define

$$m_\delta = \frac{4rr'}{(z-z')^2 + (r+r')^2 + \delta^2} \tag{3.8}$$

which bounds m_δ below by $1 + \mathcal{O}(\delta^2)$. Thus, each calculation is stopped shortly before the first singularity begins to appear, and m is replaced by m_δ in the equations of motion (1.1), (1.2) for the remainder of the computation. As the integrands are now smoothed, special quadrature methods are unnecessary, and full trapezoidal rule is used. More importantly, the 'δ-smoothing' removes the unboundedness of the growth rates at large k. In the case of 2D planar sheets it has also been shown that an analogous regularization gives global analyticity of the sheet motion [6]. While smoother data, or the inclusion of viscosity, are more natural regularizations, it has been seen that 'δ-smoothing' captures the qualitative features of smoother flows [13]. For the computations described below, the validity of the results with δ-smoothing will be demonstrated by carefully assessing the effect of varying δ.

As shown in section 5, the arclength of the vortex sheet goes to infinity. Therefore, in addition to the parameters N, M, Δt, δ, a set of interpolation criterion tolerances η_z, η_r and η_ψ are needed. In particular, we require that $|z_{j+1} - z_j| < \eta_z$, $|r_{j+1} - r_j| < \eta_r$, $|\psi_{j+1} - \psi_j| < \eta_\psi$ for every pair of neighbouring points (z_j, r_j, ψ_j) and $(z_{j+1}, r_{j+1}, \psi_{j+1})$ at each time step. The typical values for $(\eta_z, \eta_r, \eta_\psi)$ are $(0.1, 0.0375, 0.1)$. If two points (z_j, r_j, ψ_j) and $(z_{j+1}, r_{j+1}, \psi_{j+1})$ fail the requirement, we insert a point in the middle by placing it on a cubic polynomial which is fit to the neighbouring four points $\{(z_k, r_k, \psi_k) | k = j-1, j, j+1, j+2\}$.

4. Computation of a single cylindrical swirling vortex sheet

The first computations using the method of the previous section were performed on the linearly stable problem of a single cylindrical, swirling vortex sheet. The unperturbed vortex

sheet has radius $R_0 = 1$ and circulation $\Gamma = -2\pi$. An initial perturbation is added which is an exact eigenfunction corresponding to a standing wave. The evolution is governed by equations (1.1)–(1.3).

From (2.30) with $\Gamma_1 = 0$ and $\Gamma_2 = -2\pi$ the linearized mode for a standing wave with $k = 1$ is (z', r', ψ') given by

$$(z', r', \psi') = (a_1 \sin\alpha \cos\omega t,\ a_2 \cos\alpha \cos\omega t,\ a_3 \cos\alpha \sin\omega t) \tag{4.1}$$

in which

$$a_1 = -0.770\,355 \qquad a_2 = 1.0 \qquad a_3 = 1.714\,549 \qquad \omega = 0.583\,244. \tag{4.2}$$

Thus the initial data for this computation are

$$z = \alpha + \varepsilon a_1 \sin\alpha \qquad r = R_0 + \varepsilon a_2 \cos\alpha \qquad \psi = 0 \tag{4.3}$$

in which the amplitude ε is chosen to be $\varepsilon = 10^{-3}$, small enough that linear theory is valid. The resulting solution serves as a check on the analytical and numerical formulation and implementation.

The computation is performed in double precision using Krasny filtering at a level $\varepsilon_f = 10^{-11}$, with no desingularization ($\delta = 0$) since no singularities formed. The computation used $N = 512$ points, $M = 4$ (9 periods) and the time step $\Delta t = 0.010\,773$. For this small amplitude, the computation works equally well without Krasny filtering.

For z and r respectively, figures 4.1(a) and (b) show that the initial data (full curve) and the solution after one period $T = 10.772\,828$ are indistinguishable. The agreement of z and r at $t = 0$ and $t = T$ shows that the solution is correctly simulated.

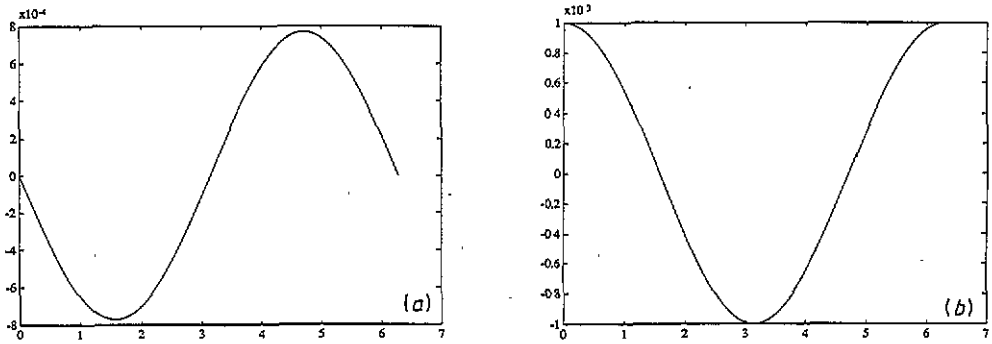

Figure 4.1. Comparison of initial data and solution after one period, which are indistinguishable, for a single cylindrical vortex sheet with small initial perturbation, with $\delta = 0.0$. The perturbation in height $z - \alpha$ against the Lagrangian parameter α is plotted in (a), and the perturbation in radius $r - 1$ is plotted in (b).

The computational result for a perturbation of larger amplitude $\varepsilon = 0.6$ is shown in figure 4.2. In this solution the outward jet has begun to significantly distort due to Kelvin–Helmholtz instability, destroying the periodicity of the solution. This phenomenon is also observed in the computations of the next section, where it will be discussed in detail.

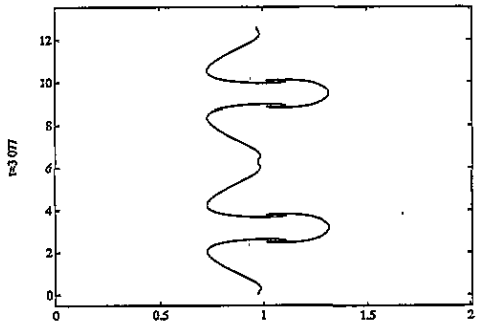

Figure 4.2. Development of rolled-up jets for a single cylindrical vortex sheet with perturbation of large amplitude. This profile is irreversible, so that the motion is not periodic.

5. Computation of an axi-symmetric swirling vortex sheet with a line vortex on symmetry axis

5.1. Evolution of a linearly unstable vortex sheet

In this section, we will consider an axi-symmetric vortex sheet with a line vortex along the symmetry axis. Denote the circulation inside the sheet and outside the sheet by Γ_1 and Γ_2, respectively. Because of its symmetry the line vortex does not move.

Since the circulation of the sheet is $\Gamma_s = \Gamma_2 - \Gamma_1$, the Lagrangian equations of motion for the sheet are (with Γ replaced by Γ_s in the r, z equations, and by $\Gamma_1 + \Gamma_2$ in the ψ equation)

$$\begin{aligned} z_t &= \frac{\Gamma_2 - \Gamma_1}{2\pi^2} PV \int I_1(r, r', z - z', \psi')\, d\alpha' \\ r_t &= \frac{\Gamma_2 - \Gamma_1}{2\pi^2} PV \int I_2(r, r', z - z', \psi')\, d\alpha' \\ \psi_t &= (\Gamma_1 + \Gamma_2)(4\pi r^2)^{-1}. \end{aligned} \tag{5.1}$$

For this problem, the sheet is linearly unstable if and only if $\Gamma_1^2 > \Gamma_2^2$ according to Rayleigh's criterion. We choose a linear unstable Lagrangian mode as initial data, derived in section 2.5.2. In particular, let $R_0 = 1$, $\Gamma_1 = 6$, $\Gamma_2 = 6 - 2\pi$, $k = 1$ in (2.27) and (2.30), and choose initial amplitude $\varepsilon = 0.1$:

$$\begin{cases} z(t = 0) = \alpha + \varepsilon c_1 \sin\alpha \\ r = 1 + \varepsilon \cos\alpha \\ \psi = \varepsilon c_2 \cos\alpha \end{cases} \tag{5.2}$$

in which $c_1 = -0.77$, $c_2 = -1.6$.

The equations (5.1) are solved by the methods described in section 3 with $N = 512$, $M = 4$, and time step $\Delta t = 0.005$.

The plots in figures 5.1–5.6 are vertical cross sections of two periods in z for the cylinder at successive times. As discussed in section 2.6, the unstable Lagrangian mode produces axial flows which send fluid into the regions where the cylinder bulges and out of those where it pinches (figures 5.1–5.3). This motion forms an incoming jet towards the symmetry axis

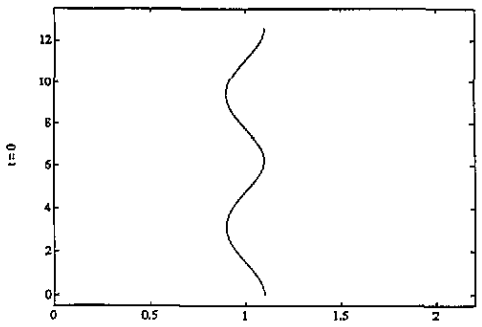

Figure 5.1. Profile z (height) against r (radius) at $t = 0.0$ for a perturbed cylindrical vortex sheet with a vortex line on the axis of symmetry ($r = 0$). The perturbation of the initial data shown here is chosen to be a linearly unstable mode. The horizontal scale is quite exaggerated in figures 5.1–5.6.

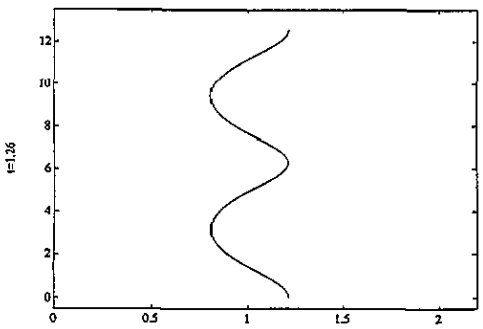

Figure 5.2. Same as figure 5.1 but at $t = 1.26$. $\delta = 0.0$. Note the formation of inward and outward jets.

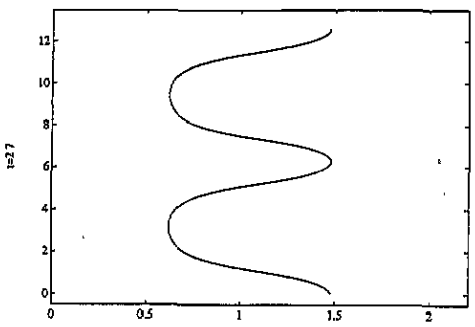

Figure 5.3. Same as figure 5.1 but at $t = 2.7$, showing broadening of the inward jet. $\delta = 0.0$.

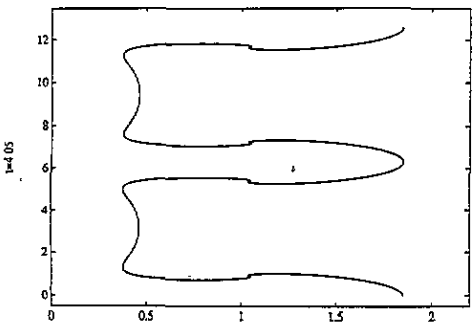

Figure 5.4. Same as figure 5.1 but at $t = 4.05$, showing splitting of the inward jet and the beginning of roll-up on the outward jet. $\delta = 0.1$.

and an outgoing jet away from the axis in each axial period. Simultaneously, this collapse causes the vortex lines to be pulled around the axis more rapidly where the cylinder is narrower (i.e. $z = \pi$), and there is substantial stretching and realignment of vorticity into the azimuthal direction. This is vorticity for which the Kelvin–Helmholtz instability is operative, and at $t \approx 2.7$ (figure 5.3), we observe a curvature singularity presumably related to that seen in 2D vortex sheet motion [14, 15, 17, 18, 25]. This curvature singularity for an axi-symmetric vortex sheet has been studied in detail by Pugh and Cowley [21]. As described in section 3, for $t > 2.7$, the δ-regularization is introduced together with the usual trapezoidal quadrature.

Proceeding on, figure 5.4 shows splitting of the tip of the incoming jet and roll-up on the neck of the outgoing jet for $\delta = 0.1$. The roll-up is a result of the Kelvin–Helmholtz instability in the z–r plane induced by angular vorticity on the sheet. In figure 5.5, the stem of the outgoing jet sheet pinches further together, the tips of the incoming jet continue to move towards the axis, and the roll-up proceeds smoothly. Figure 5.6 shows the configuration of the vortex sheet at the end of the computation. The sheet is further

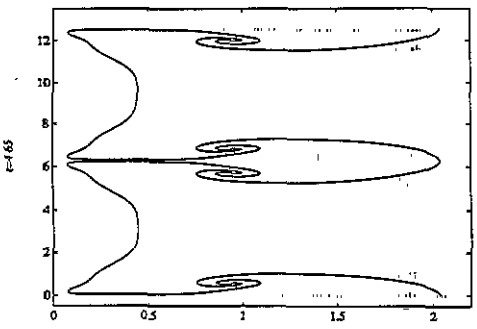

Figure 5.5. Same as figure 5.1 but at $t = 4.65$. Note the narrowing of the stem to the outward jet and the further roll-up. $\delta = 0.1$.

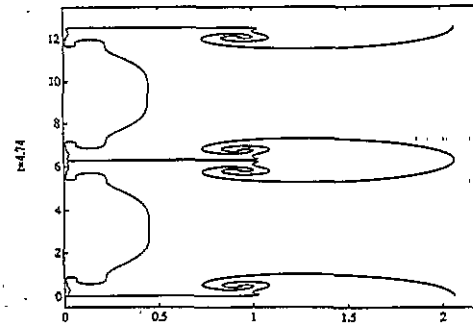

Figure 5.6. Same as figure 5.1 but at $t = 4.74$. $\delta = 0.1$. The inward jet has split a second time and nearly hit the vortex line on $r = 0$. The stem of the outward jet has nearly collapsed.

pinched together at the stem of the outgoing jet, the tips of the incoming jet are yet closer to the axis, and each tip has split a second time.

The computation stops at this time because the sheet configuration has become complicated and difficult to accurately represent. Since the minimum radius of the sheet is nearly zero, the angular velocity ψ_t is very large, and the vortex lines on the sheet are tightly wound up. Moreover, since the vorticity density is $r^{-1}(r_\alpha^2 + z_\alpha^2)^{-\frac{1}{2}}(\Gamma_s/2\pi)(z_\alpha, r_\alpha, r\psi_\alpha)$ in cylindrical coordinate (z, r, θ), the vorticity density blows up when the radius goes to zero. This collapse and singularity formation is caused by vortex stretching that produces angular vorticity and radial jets.

The collapse of the vortex sheet onto $r = 0$ could also be interpreted as (partial) vortex cancellation between vortex lines on the sheet and the central vortex line. Since the computations stop slightly before this collapse occurs, further details of the cancellation are not discernible.

A second cancellation occurs as the vortex sheet hits itself along the stem of the outward jet. Note that the vortex sheet stays symmetric with respect to planes $z = 2\pi$ (or any periodic image of 2π) where this collision occurs. At points (z_1, r_1, ψ_1) and (z_2, r_2, ψ_2) that are symmetric about the plane $z = 2\pi$, i.e. $z_2 = 2\pi - z_1$, $r_2 = r_1$, $\psi_2 = \psi_1$, the derivatives are $(z_{1\alpha}, r_{1\alpha}, \psi_{1\alpha}) = -(z_{2\alpha}, r_{2\alpha}, \psi_{2\alpha})$. Thus the vorticity vectors are equal and opposite at these points; so that during this event the vorticity cancels along the pinching stem of the outgoing jet. Therefore the outgoing jet forms a vortex ring that is detached from the rest of the sheet.

Note that the vortex blob method could be interpreted as a vortex sheet with 'thickness' δ. Therefore, it desingularizes the collision of the sheet with itself and the collision does not actually appear in the computation. Finally, figure 5.7 shows that the arclength of the vortex line goes to ∞ as the sheet evolves in time. This requires addition of new points on a vortex line after a certain time using the tolerances η, as described in section 3.

5.2. *Sensitivity to numerical parameters*

For fixed $\delta = 0.1$, the graphs presented in section 5.1 are not significantly altered if Δt is decreased or M is increased. Variation in the number of points N is slightly more subtle since points will be automatically inserted, as described in section 3. Consider two computations with initial values of $N = 512$ and $N = 1024$, and with values of the insertion

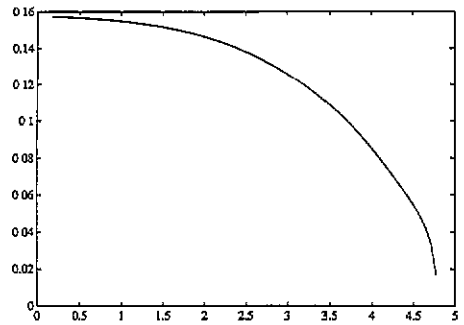

Figure 5.7. Inverse of the arclength for a vortex line against time in the computation of figures 5.1–5.6. Rapid growth of the arclength requires addition of new computational points.

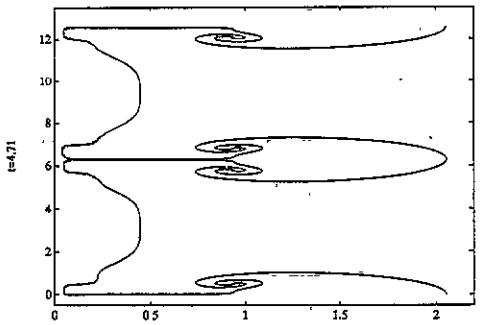

Figure 5.8. Comparison of the computation of figures 5.1–5.6 (full curve), in which the initial number of points is $N = 512$, with a refined computation (broken curve) for which $N = 1024$. $\delta = 0.1$.

parameters η for the 1024 computation equal to half their values for the 512 computation. The sheet positions are detectably different only for $t \geqslant 4.5$. Figure 5.8 at $t = 4.71$ shows slight differences in the region where many points have been inserted.

Figures 5.9(a) shows that the minimum radius $r_{\min}$ of the sheet goes to zero at a rate that is similar for different δ values. Figure 5.9(b) shows the minimum distance $d_{\min}$ between the two sides of the stem of the outer jet, which also goes to zero at a rate that is similar for different δ values. Since the speed of vortex sheet motion increases as the blob size δ is decreased, the collapse of $r_{\min}$ and $d_{\min}$ occurs earlier for smaller δ. We also found that the horizontal velocities inside the stem became very large as it pinched. It was, however, difficult to quantify whether these velocities or their associated mass fluxes were actually diverging as the blob size was decreased.

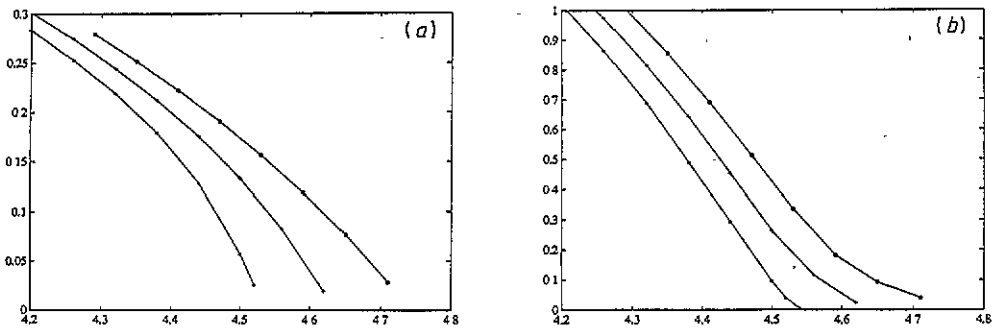

Figure 5.9. Dependence on the value of the desingularization parameter δ for (a) the minimum radius $r_{\min}$ of the sheet, and (b) the minimum distance $d_{\min}$ between the sides of the stem for the outgoing jet. The values of δ are 0.1 (○), 0.075 (+), and 0.05 (∗). Note that the collapse of both $r_{\min}$ and $d_{\min}$ occurs earlier for smaller δ.

Finally, the vortex sheet profiles are compared for two different values of δ. Since the velocity is large for r near 0, which is the most interesting region in this comparison, small differences between the solutions can easily be amplified. In order to show a meaningful

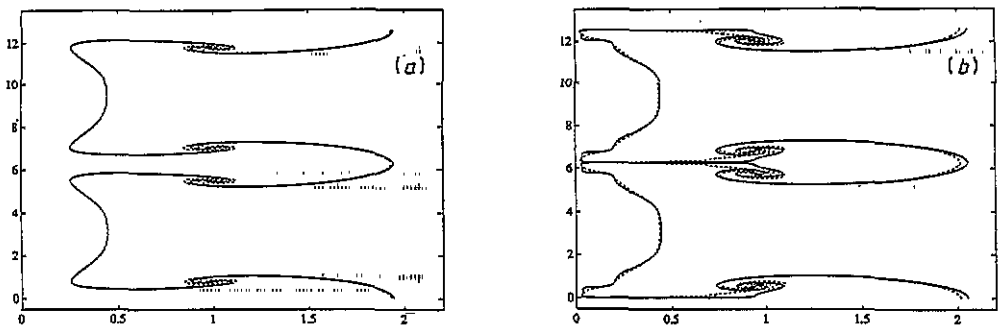

Figure 5.10. Dependence of the vortex sheet profile on δ at (a) an early time and (b) a later time. The values of δ are 0.1 (full curve) and 0.05 (broken curve). The times for the two computations are chosen so that $r_{\min}$ is the same: $t = 4.35$ for $\delta = 0.1$ and $t = 4.26$ for $\delta = 0.05$ in (a); $t = 4.71$ for $\delta = 0.1$ and $t = 4.52$ for $\delta = 0.05$ in (b).

agreement between the two computations for $\delta = 0.1$ and $\delta = 0.05$, we compare the two solutions at times for which the values of $r_{\min}$ are the same. Figures 5.10(a) and (b) show this comparison at two values of $r_{\min}$. The shape of the vortex sheet is seen to be roughly independent of δ.

Together with the comparison of $r_{\min}$ and $d_{\min}$ at different values of δ in figures 5.9(a) and (b), this shows that the qualitative features of the flow, including collapse and pinchoff, are independent of δ.

6. Computation of two axi-symmetric swirling vortex sheets

If the vortex line in the computations of section 5 is replaced by an axi-symmetric vortex sheet of small radius and with the same circulation, then the initial motion of the outer vortex sheet will be nearly unchanged. As the radius outer vortex sheet collapses, however, the two sheets will start to interact in a non-trivial way.

In these computations the background steady flow is that due to an inner cylindrical vortex sheet of radius 0.1 with circulation $\Gamma_1 = -2\pi$ and an outer cylindrical vortex sheet of radius 1.0 with circulation $\Gamma = \Gamma_2 - \Gamma_1 = 2\pi$. The circulation outside the outer sheet is thus $\Gamma_2 = 0$, so that the configuration is unstable according to Rayleigh's criterion. Following the linear stability analysis of section 2, an unstable mode of amplitude 0.1 on the outer sheet is added to this steady state. The initial data are thus

$$z_I = \alpha - 0.090\,868 \sin\alpha \qquad r_I = 0.1 + 0.000\,061 \cos\alpha \qquad \psi_I = 0.104\,298 \cos\alpha \quad (6.1)$$

$$z_O = \alpha - 0.077\,83 \sin\alpha \qquad r_O = 1.0 + 0.1 \cos\alpha \qquad \psi_O = 0.171\,917 \cos\alpha. \quad (6.2)$$

The evolution equations for these two sheets are generalized from (1.1)–(1.3) as

$$\partial_t z_I = \frac{\Gamma_1}{2\pi^2} PV \int I_1(r_I, r_I', z_I - z_I', \psi_I')\, d\alpha' + \frac{\Gamma}{2\pi^2} \int I_1(r_I, r_O', z_I - z_O', \psi_O')\, d\alpha' \quad (6.3)$$

$$\partial_t r_I = \frac{\Gamma_1}{2\pi^2} PV \int I_2(r_I, r_I', z_I - z_I', \psi_I')\, d\alpha' + \frac{\Gamma}{2\pi^2} \int I_2(r_I, r_O', z_I - z_O', \psi_O')\, d\alpha' \quad (6.4)$$

$$\partial_t \psi_I = \Gamma_1/(4\pi r_I^2) \tag{6.5}$$

$$\partial_t z_O = \frac{\Gamma}{2\pi^2} PV \int I_1(r_O, r'_O, z_O - z'_O, \psi'_O)\,\mathrm{d}\alpha' + \frac{\Gamma_1}{2\pi^2} \int I_1(r_O, r'_I, z_O - z'_I, \psi'_I)\,\mathrm{d}\alpha' \tag{6.6}$$

$$\partial_t r_O = \frac{\Gamma}{2\pi^2} PV \int I_2(r_O, r'_O, z_O - z'_O, \psi'_O)\,\mathrm{d}\alpha' + \frac{\Gamma_1}{2\pi^2} \int I_2(r_O, r'_I, z_O - z'_I, \psi'_I)\,\mathrm{d}\alpha' \tag{6.7}$$

$$\partial_t \psi_O = (\Gamma_1 + \Gamma_2)/(4\pi r_O^2) \tag{6.8}$$

in which I_1 and I_2 are defined in (1.4).

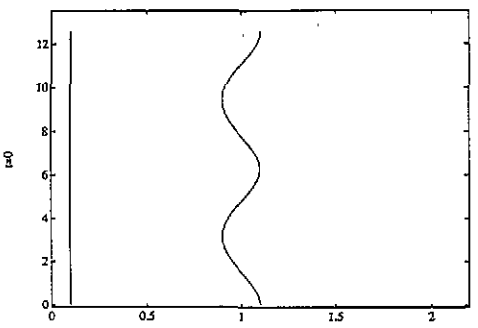

Figure 6.1. Profile z (height) against r (radius) at $t = 0.0$ for a configuration of two co-axial, perturbed cylindrical vortex sheets. In this computation the initial radii of the two sheets are very different.

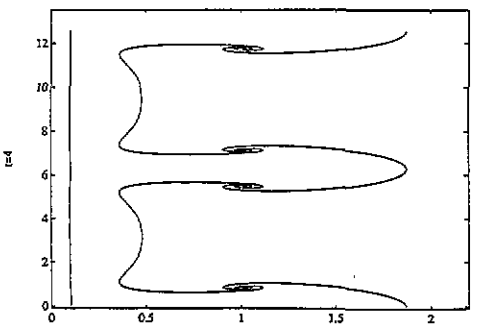

Figure 6.2. Same as figure 6.1 but at $t = 4.0$. $\delta = 0.05$. The outer sheet has formed jets and roll-up as in the computation of section 5.

Equations (6.3)–(6.8) with initial data (6.1)–(6.2) were numerically solved using the method described in section 3 with $N = 512$ numerical points, $M = 3$, desingularization parameter $\delta = 0.05$, time step $\Delta t = 0.01$, and point insertion parameters $(\eta_{zI}, \eta_{rI}) = (0.03, 0.001)$ for the inner sheet and $(\eta_{zO}, \eta_{rO}) = (0.06, 0.038)$ for the inner sheet. No point insertion parameter η_θ was needed. Desingularization was used throughout the computation. For consistency and simplicity, all of the integrals in equations (6.3)–(6.7) were desingularized throughout the computation.

The numerical results of this computation are displayed in figures 6.1–6.6. In the first two figures 6.1 and 6.2, the initial unstable amplification and the formation of an outward jet with Kelvin–Helmholtz rolls are displayed and are almost exactly the same as the corresponding results for a vortex sheet and a line vortex in figures 5.1 and 5.2. Note that since the external flow fields for a line vortex and an unperturbed cylindrical sheet are identical, the difference in the behaviour of the outer sheet in the two cases is initially proportional to the deformation of the inner sheet.

When the outer sheet approaches the inner sheet, as portrayed in figure 6.3 and continued in figures 6.4 and 6.5, a strong interaction develops between them. In figures 6.3–6.5, the first figure (*a*) shows the overall shape of the two sheets and the second figure (*b*) is a magnification of the interaction region. At first, the inner sheet is pushed inward by the inward radial jet of the outer sheet, as in figure 6.3 at $t = 4.5$. Then rolls in the outer sheet begin to form on the sides of the inward jet and the inner sheet gets entrained into these rolls, as in figure 6.4 at $t = 4.55$. The last figure 6.5 at $t = 4.6$, shows the two vortex sheets

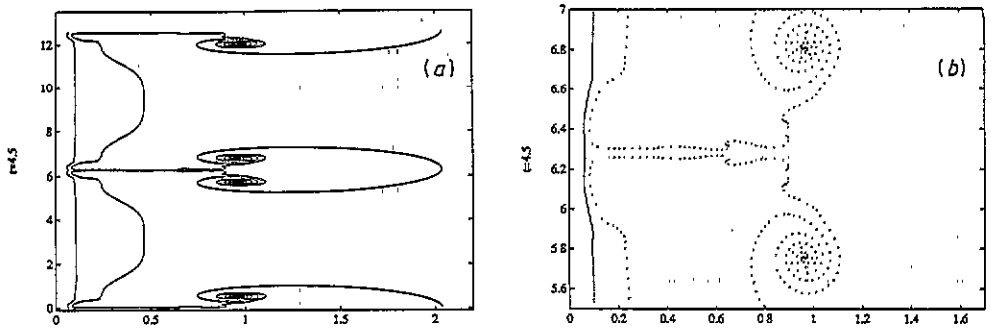

Figure 6.3. Same as figure 6.1 but at $t = 4.5$. $\delta = 0.05$ The inner sheet has begun to deform as it is hit by the inner jets of the outer sheet. A detailed view of the region of interaction between the sheets is provided in (*b*).

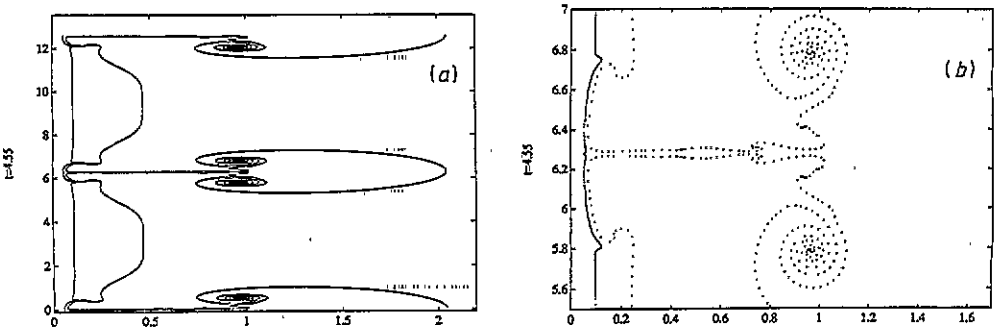

Figure 6.4. Same as figure 6.1 but at $t = 4.55$. $\delta = 0.05$.

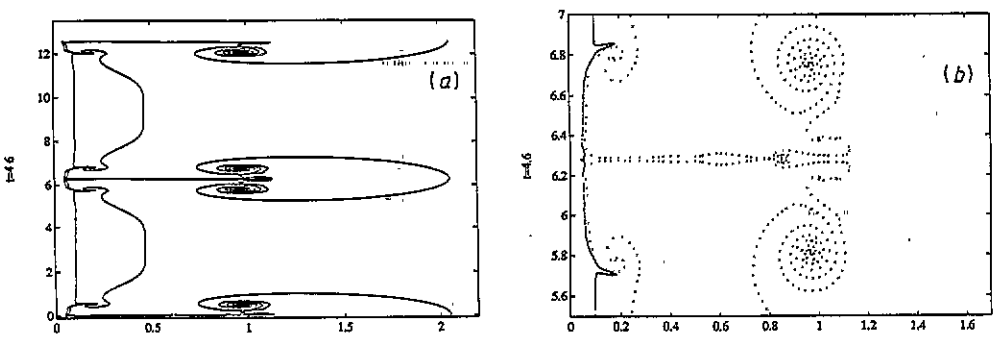

Figure 6.5. Same as figure 6.4 but at $t = 4.6$. $\delta = 0.05$.

to be almost exactly aligned (i.e. $r_O = r_I, z_O = z_I$) in their interaction region. Unlike the previous case of a single sheet interacting with the line vortex, no collapse onto the axis is observed. Although the computation presented here is for equal and opposite values of the circulation on the two sheets, this alignment of the sheets (but not of the vorticity vectors) still occurs if the circulation values are not equal.

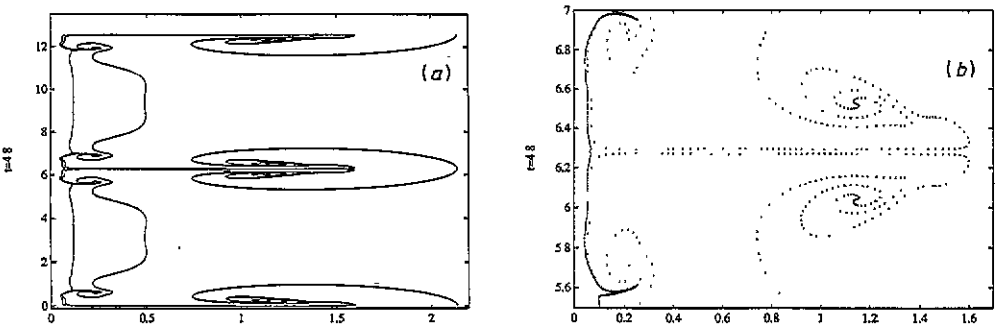

Figure 6.6. Same as figure 6.4 but with $\delta = 0.1$ and at $t = 4.8$.

Although the configuration at these late times is quite complicated, the vortex sheet curves are well resolved, as seen in figures 6.3(b), 6.4(b) and 6.5(b). Moreover the results for $\delta = 0.1$ presented in figure 6.6 are very close qualitatively to the results for $\delta = 0.05$. The main difference for two different values of δ is a time delay for larger δ, as discussed in detail in section 5.

As the two sheets align there is cancellation of their r and z vorticity, but not their θ vorticity, as shown in figure 6.7. The values of the z-component σ_z^I for the inner sheet and the negative of the z-component for the outer sheet are plotted against z in figure 6.7(a). The analogous plot for the r-components σ_r^I and σ_r^O is in figure 6.7(b). Figure 6.7(c) shows that there is no relation between σ_θ^I and σ_θ^O.

This cancellation is expected according to the following argument: For the z-component, consider the circulation Γ_ℓ around a circular loop outside the two sheets. Since the net circulation vanishes, $\Gamma_\ell = 0$. On the other hand, Stokes theorem says that Γ_ℓ is equal to the integral of ω_z over the horizontal disc bound by their loop. Since the surface area of the sheet per unit height in z is $2\pi r\sqrt{1 + r_\alpha^2/z_\alpha^2}$, this integral is

$$\Gamma_\ell = \sigma_z^I 2\pi r_I \sqrt{1 + r_{I\alpha}^2/z_{I\alpha}^2} + \sigma_z^O 2\pi r_O \sqrt{1 + r_{O\alpha}^2/z_{O\alpha}^2}. \tag{6.9}$$

When the two sheets are aligned then $r_I = r_O$ and $(r_{I\alpha}/z_{I\alpha})^2 = (r_{O\alpha}/z_{O\alpha})^2$ so that

$$\sigma_z^I = -\sigma_z^O. \tag{6.10}$$

For the r-components suppose that the two sheets are nearly aligned and not vertical. Consider two loops of the same radius, one inside the inner sheet and the other outside the outer sheet, both of which have zero circulation so that the total circulation is $\Gamma_\ell = 0$. Apply Stokes theorem using the cylindrical section bound by these two loops. As in (6.9) the integral of ω_r over this section is

$$\Gamma_\ell = \sigma_r^I 2\pi r_I \sqrt{1 + z_{I\alpha}^2/r_{I\alpha}^2} + \sigma_r^O 2\pi r_O \sqrt{1 + z_{O\alpha}^2/r_{O\alpha}^2}. \tag{6.11}$$

As before this implies

$$\sigma_r^I = -\sigma_r^O \tag{6.12}$$

if the two sheets are aligned. This anti-alignment of the vorticity vectors can only occur if the circulation values of the two sheets are equal and opposite.

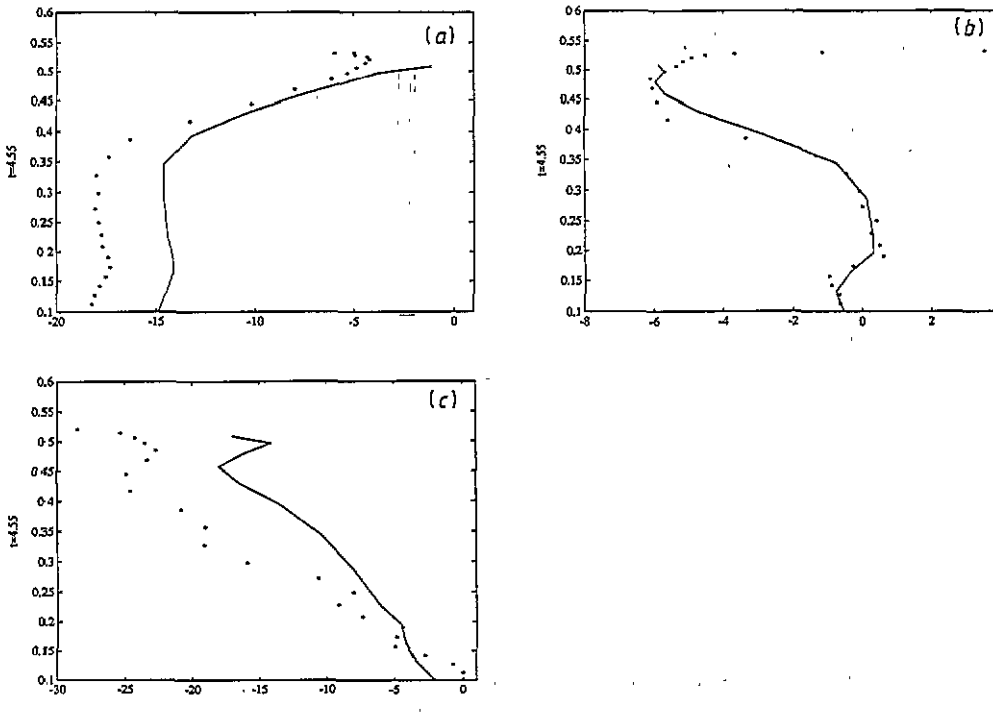

Figure 6.7. Comparison of (*a*) the z-components, (*b*) the r-components and (*c*) the θ-components of the vorticity vector on the inner sheet (*) and the outer sheet (full curve) at $t = 4.55$ as a function of z. Note that in regions where the two sheets align, the z- and r-components are equal.

A very different evolution occurs if the radius of the inner sheet is not small. Consider a steady configuration with inner radius 1 and outer radius 1.5 and perturb with the unstable mode to get initial data

$$z_I = \alpha - 0.119\,007 \sin\alpha \qquad r_I = 1. + 0.015\,975 \cos\alpha \qquad \psi_I = 0.051\,564 \cos\alpha$$

$$z_O = \alpha - 0.077\,275 \sin\alpha \qquad r_O = 1.5 + 0.1 \cos\alpha \qquad \psi_O = 0.095\,639 \cos\alpha.$$

The solution of equations (6.3)–(6.8) is presented in figures 6.8-6.10 for these initial data.

The first figure 6.8 shows the linear growth of inward and outward jets on the two sheets, as expected. Because the radius of the inner sheet is relatively large compared to that in the previous computation, the amplitude of the perturbation is also much larger. As the outward jet on the outer sheet starts to pull away and roll-up, the inner sheet is entrained into the stem of the outward jet on the outer sheet, as seen in figure 6.9. The inner sheet then begins to roll-up inside of this stem and the main interaction of the two sheets occurs along this stem, as seen in figure 6.10, in contrast to the earlier computation.

7. Conclusion

Axi-symmetric vortex sheets are a special class of solutions that may be studied to gain insight into three-dimensional fluid flow. Our investigation demonstrates that analysis and

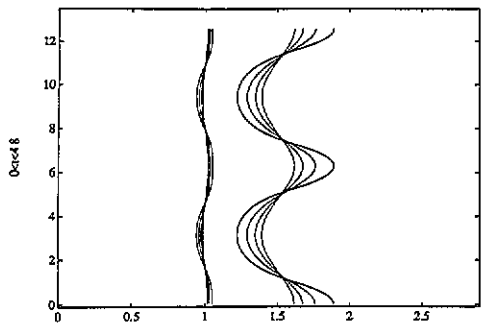

Figure 6.8. Profile z (height) against r (radius) at $t = 0.0$ for a configuration of two co-axial, perturbed cylindrical vortex sheets. In this computation the initial radii of the two sheets are not very different.

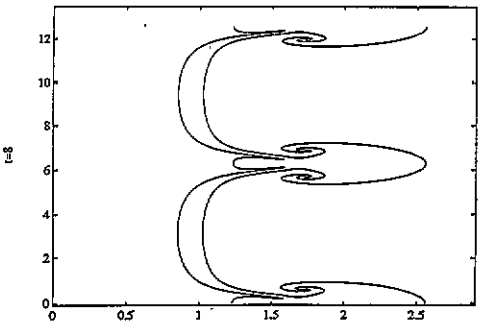

Figure 6.9. Same as in figure 6.8 but at $t = 8.0$. Note that the inner sheet is entrained into the outgoing jet of the outer jet, in contrast to the behaviour of the sheets in computation of figures 6.1–6.6.

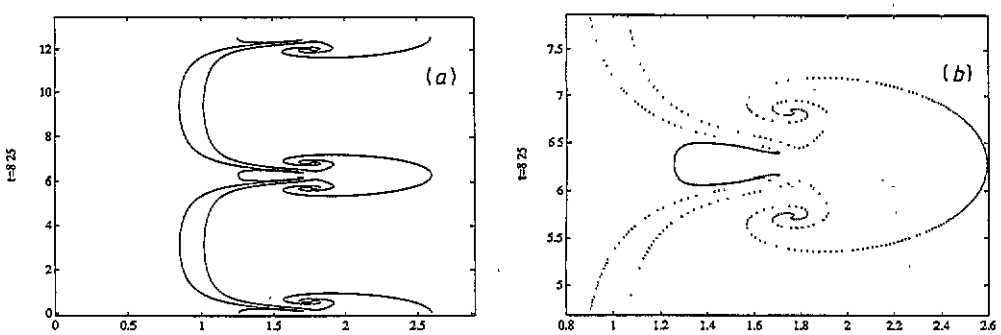

Figure 6.10. Same as in figure 6.8 but at $t = 8.25$. A detailed view of the region of interaction between the sheets is provided in (*b*).

computation for such flows can be performed in a relatively straightforward manner. A number of phenomena emerge from this study:

Instability occurs for a system of axi-symmetric vortex sheets if Rayleigh's criterion is met. Due to the simplicity of these flows, explicit expressions are found for the unstable growth rate (or the frequency in the stable case) and for the linear modes.

Although there are singularities and numerical difficulties in the vortex sheet formulation, an effective numerical method has been developed for this problem. The method is stabilized through use of Krasny filtering before the first roll-up singularity and δ-desingularization afterwards. Although it is not possible to make δ smaller than 0.01, the main features of the flow are seen to be independent of δ.

The numerical results show the formation of inward and outward jets, along with winding up and stretching of the vortex lines, as predicted by linear theory. Further computation shows a number of nonlinear effects in the unstable cases. The tip of the inward jet splits into two. Furthermore, in the case of a vortex sheet and an axial vortex line, the inward jet drives the vortex sheet to collapse onto the vortex line at some points; while for two vortex sheets, the outer sheet is driven into the inner one. This process may be interpreted as vortex cancellation, and in the case of the collapse onto the axis it is

accompanied by blow-up of the vorticity density.

A second collision take place between the vortex sheet and itself along the stem of the outward jet. Due to the symmetry in these problems, the vorticity exactly cancels where it hits. The result is detachment of an outer vortex ring.

Acknowledgments

The authors wish to thank Robert Krasny, Eckart Meiburg and Alain Pumir for useful conversations.

References

[1] Abramowitz M and Stegun I A 1970 *Handbook of Mathematical Functions* (New York: Dover) p 374
[2] Baker G R and Shelley M J 1990 On the connection between thin vortex layers and vortex sheets *J. Fluid Mech.* **215** 161–94
[3] Caflisch R E 1993 Singularity formation for complex solutions of the 3D incompressible Euler equations *Physica* **67D** 1–18
[4] Caflisch R E, Hou Thomas Y and Lowengrub J Convergence of a nonlinear filtering method *Preprint*
[5] Caflisch R E and Xiaofan Li 1992 Lagrangian theory for 3D vortex sheets with axial or helical symmetry *Transport Theor. Stat. Phys.* **21** 559–78
[6] Caflisch R E and Lowengrub J S 1989 Convergence of the vortex method for vortex sheets *SIAM J. Num. Anal.* **26** 1060–80
[7] Chen C F, Liu D C S and Skok M W 1973 Stability of circular Couette flow with constant finite acceleration *J. Appl. Mech.* **40** 347–54
[8] Dahm W J A and Frieler C E and Tryggvason G 1992 Vortex structure and dynamics in the near field of a coaxial jet *J. Fluid Mech.* **241** 371–402
[9] de Bernardinis and Moore D W A 1986 A ring-vortex representation of an axi-symmetric vortex sheet *Studies of Vortex Dominated Flows* ed M Y Hussain and M D Salas (Berlin: Springer)
[10] Drazin P G and Reid W H 1981 *Hydrodynamic Stability* (Cambridge: Cambridge University Press) ch 3
[11] Grauer R and Sideris T Numerical computation of 3d incompressible ideal fluids with swirl *Phys. Rev. Lett.* **25** 3511–14
[12] Kirchner R P and Chen C F 1970 Stability of time-dependent rotational Couette flow. Part 1. Experimental investigation *J. Fluid Mech.* **40** 39–47
[13] Krasny R 1986 Desingularization of periodic vortex sheet roll-up *J. Comput. Phys.* **65** 292–313
[14] Krasny R 1986 A study of singularity formation in a vortex sheet by the point-vortex approximation *J. Fluid Mech.* **167** 65–93
[15] Meiron D I, Baker G R and Orszag S A 1982 Analytic structure of vortex sheet dynamics, part 1, Kelvin–Helmholtz instability *J. Fluid Mech.* **114** 283–98
[16] Meiron D I and Shelley M J 1992 Personal communication
[17] Moore D W 1985 The spontaneous appearance of a singularity in the shape of an evolving vortex sheet *Proc. R. Soc.* A **365** 105–19
[18] Moore D W 1985 Numerical and analytical aspects of Helmholtz instability *Proc. XVI ICTAM, Theoretical and Applied Mechanics* ed Niordson and Olhoff (Amsterdam: North-Holland) pp 629–33
[19] Nitsche M 1992 Axisymmetric vortex sheet roll-up *Thesis* Department of Mathematics, The University of Michigan
[20] Pugh D A 1989 Development of vortex sheets in Boussinesq flows—formation of singularities *PhD Thesis* Imperial College
[21] Pugh D A and Cowley S J 1993 On the formation of an interface singularity in the rising 2D Boussinesq bubble *J. Fluid. Mech.* in press
[22] Pumir A and Siggia E D 1992 Development of singular solutions to the axisymmetric Euler equations *Phys. Fluids* A **4** 1472–91
[23] Lord Rayleigh 1916 On the dynamics of revolving fluids *Proc. R. Soc.* A **93** 148–54
[24] Rotunno R 1978 A note on the stability of a cylindrical vortex sheet *J. Fluid Mech.* **87** 761–71
[25] Shelley M J 1992 A study of singularity formation in vortex sheet motion by a spectrally accurate vortex method *J. Fluid Mech.* **244** 493–526

[26] Shelley M J and Meiron D I and Orszag S A 1993 Dynamical aspects of vortex reconnection of perturbed anti-parallel vortex tubes *J. Fluid Mech.* **246** 613–52
[27] Shelley M J and Vinson M 1992 Coherent structures on a boundary layer in Rayleigh–Benard turbulence *Nonlinearity* 5 323–51
[28] Sidi A and Israeli M 1988 Quadrature methods for periodic singular and weakly singular Fredholm integral equations *J. Sci. Comput.* 3 201–31
[29] Stoer J and Burlisch R 1980 *Introduction to Numerical Analysis* (New York: Springer)
[30] Tryggvason G 1988 Numerical simulations of the Rayleigh–Taylor problem *J. Comput. Phys.* **75** 253–82
[31] Van Dyke M 1982 *An Album of Fluid Motion* (Stanford, CA: Parabolic Press) p 72